

SDD-4DGS: Static-Dynamic Aware Decoupling in Gaussian Splatting for 4D Scene Reconstruction

Dai Sun[&], Huhao Guan[&], Kun Zhang[&], Xike Xie[✉], S. Kevin Zhou^{✉*}
 School of Biomedical Engineering, Division of Life Sciences and Medicine,
 University of Science and Technology of China, Hefei, Anhui, 230026, P.R.China

Abstract

Dynamic and static components in scenes often exhibit distinct properties, yet most 4D reconstruction methods treat them indiscriminately, leading to suboptimal performance in both cases. This work introduces SDD-4DGS, the first framework for static-dynamic decoupled 4D scene reconstruction based on Gaussian Splatting. Our approach is built upon a novel probabilistic dynamic perception coefficient that is naturally integrated into the Gaussian reconstruction pipeline, enabling adaptive separation of static and dynamic components. With carefully designed implementation strategies to realize this theoretical framework, our method effectively facilitates explicit learning of motion patterns for dynamic elements while maintaining geometric stability for static structures. Extensive experiments on five benchmark datasets demonstrate that SDD-4DGS consistently outperforms state-of-the-art methods in reconstruction fidelity, with enhanced detail restoration for static structures and precise modeling of dynamic motions. The code will be released.

1. Introduction

Reconstruction technology is vital in our daily lives, with spread used in films, VR applications, and driver assistance systems, highlighting its importance in computer vision and graphics [23, 34]. Reconstruction aims to estimate a 3D scene representation from multiple 2D perspectives, facilitating realistic rendering from novel views. In contrast to conventional 3D reconstruction, which merely focuses on static scenes, 4D reconstruction constructs both the scene and its temporal information from scarce 2D observations, enabling effective modeling of the dynamic world commonly found in everyday life, thereby offering enhanced generalizability [12, 44]. Tech challenges arise since 4D reconstruction requires an additional complexity of temporal sequence modeling beyond 3D.

Recently, many impactful 4D reconstruction methods [6, 19, 37, 43] try incorporating temporal information into the

3D Gaussian Splatting (3DGS) [14], a high-fidelity rendering technique with real-time capabilities, to model dynamic scenes, showing highly promising performance. Typically, they focus on devising sophisticated modules for estimating dynamic information, *e.g.*, Deformation Net [38], and Polynomial-based Fitting [19]. Despite these advances, current research generally assumes that all components in a scene experience motion over time, overlooking the need to determine which specific components actually require dynamic modeling.

In reality, scenes are not solely composed of dynamic components; rather, static components such as buildings, streets, and walls often constitute a significant portion of the scene [4]. As depicted in Fig. 1(a), our analysis reveals that in typical scenes, static structures occupy approximately 75 – 85% of the scene volume, with dynamic objects (*e.g.*, pedestrians, vehicles) confined to a much smaller spatial region, typically less than 20% of the visible area. Based on this crucial observation, we argue that existing methods ignore the inherent difference between dynamic and static components within a scene. Using a static/dynamic agnostic modeling approach for reconstruction inevitably leads to mutual limitations between dynamic and static information, whose disadvantages are two-fold.

Firstly, *static low-frequency information impedes the optimization of dynamic high-frequency information, leading to less effective dynamic modeling.* In 4D reconstruction models, static regions often exhibit consistent characteristics over time (such as fixed textures and geometric boundaries), remaining relatively stable in modeling. Therefore, static regions are likely to be low-loss and easily optimized during the optimization process [45]. Since reconstruction models are optimized by minimizing the loss function, the model iteratively tends to fit static regions, driving parameters closer to these stable low-loss areas. As a result, static regions act as "low-energy anchors" in the model's optimization, guiding the reconstruction of dynamic objects toward these regions. This causes the optimization of dynamic parameters to be heavily influenced by static information, thereby paying less attention to dynamic objects.

^{*&}: Authors contribute equally to this work, [✉]: Corresponding authors

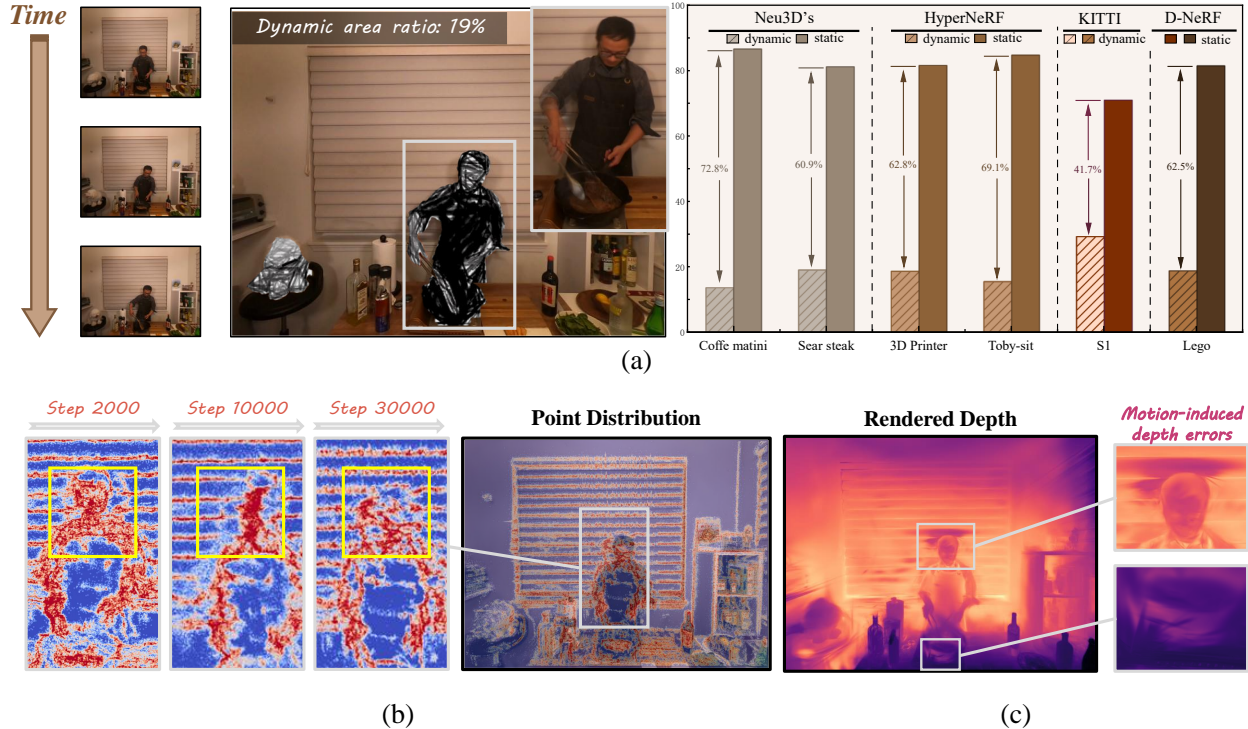


Figure 1. **Challenges in 4D scene reconstruction:** (a) Scenes typically consist of both static (e.g., buildings, walls) and dynamic (e.g., moving vehicles, pedestrians) components. (b) The red pixels represent the distribution of points projected onto the imaging plane by Gaussians. The darker the color, the more Gaussians are projected onto the pixel. As the iterative optimization proceeds, the points describing the dynamic information of the head are gradually attracted to the surrounding static area. (c) The presence of dynamic objects introduces occlusions and uneven lighting on static components, leading to artifacts and reducing the quality of static scene reconstruction. Static background depth estimation errors due to head movement. *Note:* Both (b) and (c) are derived from 4DGS [37].

For example, as shown in Fig. 1(b), we find that during the iterative optimization progresses, the points describing the dynamic information of the head (marked in the yellow box) are gradually attracted to the surrounding static areas, becoming increasingly blurred and difficult to model its dynamic information.

Secondly, in dynamic environments, moving objects, by their nature, occlude static regions, which results in uneven lighting scenarios. Specifically, the movement of dynamic objects can alter the direction and intensity of illumination, thus impacting the color appearance of static objects. Moreover, the high-speed movement of dynamic objects is prone to generating artifacts or motion blur during interactions with static objects. As a result, dynamic objects detrimentally influence the detail and geometric analysis of static objects, as shown in Fig. 1(c) that the estimated depth of the static background behind the dynamic head is inaccurate.

We propose SDD-4DGS, a 4D Gaussian splatting framework with Static-Dynamic aware Decoupling capabilities to address the issues above. To our knowledge, we are the first to reconstruct 4D scenes from the perspective of static-dynamic aware decoupling using Gaussian Splatting. Our approach integrates two complementary innovations:

(1) a theoretically rigorous dynamic perception coefficient derived in probabilistic form that naturally integrates into the Gaussian reconstruction pipeline, providing the mathematical foundation for component separation; and (2) a set of novel optimization strategies that effectively realize this theoretical potential in practical scenarios, addressing key implementation challenges that emerge when applying probabilistic models to complex dynamic scenes. In this manner, scenes are categorized as dynamic or static through a principled probabilistic framework and reconstructed with carefully designed optimization strategies. The integration of theory and practice makes SDD-4DGS a comprehensive solution for 4D reconstruction, greatly enhancing both accuracy and detail restoration across various reconstruction scenarios.

The contributions are summarized as follows:

- To our best knowledge, SDD-4DGS is the first framework to achieve static-dynamic aware decoupling in 4D reconstruction using Gaussian Splatting [14].
- We propose a novel dynamic perception coefficient rigorously derived in a probabilistic form.
- We present innovative strategies to tackle implementation optimization challenges while ensuring theoretical

integrity, featuring a progressive constraint schedule and an automatic supervision mechanism.

- We conduct extensive evaluations on five datasets [17, 24, 28, 29, 31] under four distinct experimental settings, achieving comparable or superior performance than previous state-of-the-art (SOTA) methods.

2. Related Works

Dynamic scene reconstruction aims to recover the dynamic scene using time-sequenced images. Traditional approaches employ point clouds [11, 21], meshes [5, 15], voxels [20, 46], and light fields [10, 13]. Contemporary methods leverage machine learning, notably through NeRF-based and Gaussian splatting-based techniques. NeRF-based methods [1, 2, 27] deliver photorealistic rendering via learnable differential volume rendering [25], yet face challenges with non-rigid deformations [39], occlusions [47], and time-varying lighting [33]. Gaussian splatting [14] represents 3D scenes through spatial distributions of Gaussian ellipsoids, offering quality and speed advantages. For dynamic scenes, approaches such as 4DGS [37] and Space-time [19] incorporate temporal data, treating time as a dimension or employing polynomial bases for motion. Solutions such as Realtime [43] and 4DRotor [6] utilize time-integrated 4D covariance matrices. However, these often neglect the stable static background, which is crucial for preserving fixed global geometric integrity.

Static-dynamic aware decoupling methods decompose the scene into static and dynamic regions. Mask-based approaches [9, 22, 40, 41] utilize binary masks to decouple dynamic and static components in scenes, improving reconstruction quality and handling specular effects distinctly. Recent self-supervised methods [3, 18, 35, 38] achieve dynamic-static scene decomposition without reliance on motion masks, enhancing reconstruction fidelity through various novel loss functions and learning mechanisms. In addition, some research has focused on synthesizing static components from dynamic scenes. The pioneering work NeRF On-the-go [32] handles complex occlusions in scenes by applying DINOv2 [26] features to predict uncertainty, although it requires extended training times. The latest work, WildGaussians [16], significantly improves the optimization speed based on 3DGS and analyzes lighting variations. However, these methods do not simultaneously model dynamic and static components and are thus not directly applicable for dynamic scene reconstruction. To the best of our knowledge, our SDD-4DGS is the first to introduce a self-supervised dynamic-static decoupling mechanism within a Gaussian-Splatting-based dynamic reconstruction approach, effectively extending 4D reconstruction methods.

3. Methodology

In this section, we begin by briefly reviewing 3D Gaussian Splatting (3DGS) [14] and its extension for dynamic scenes, 4D Gaussian Splatting (4DGS) [37], in Sec. 3.1. Then, in Sec. 3.2, we introduce SDD-4DGS for 4D scene reconstruction. Finally, in Sec. 3.3, we introduce our detailed optimization objectives.

3.1. Preliminary of 3D & 4D Gaussian Splatting

The 3D and 4D Gaussian Splatting methods efficiently reconstruct static and dynamic scenes. The 3D approach accurately represents static structures, while the 4D approach captures dynamic changes by incorporating temporal dimensions, facilitating advanced spatiotemporal modeling.

3D Gaussian Splatting (3DGS) [14] represents a 3D scene as a set of Gaussian ellipsoids, each $\mathbf{x} \in \mathbb{R}^3 \sim \mathcal{N}(\boldsymbol{\mu}, \boldsymbol{\Sigma})$ defined by a mean $\boldsymbol{\mu} \in \mathbb{R}^3$ and covariance $\boldsymbol{\Sigma} = \mathbf{R}\mathbf{S}\mathbf{S}^T\mathbf{R}^T$. Here, $\mathbf{S} = \text{diag}(s_x, s_y, s_z)$ and \mathbf{R} are quaternion-based. Furthermore, the color c using spherical harmonics (SH) and an opacity parameter α is incorporated. In sum, each 3D Gaussian ellipsoid is represented as $\mathcal{G} = \{\boldsymbol{\mu}, \mathbf{S}, \mathbf{R}, c, \alpha\}$. For rendering, 3DGS projects \mathbf{x} to 2D $\mathbf{x}^{2d} \sim \mathcal{N}(\boldsymbol{\mu}^{2d}, \boldsymbol{\Sigma}^{2d})$ via approximate projection. And then, integrating color c and opacity α , each pixel is shaded through α -blending:

$$\mathcal{I}(u, v) = \sum_{i=1}^N p_i(u, v) \alpha_i c_i(d_i) \prod_{j=1}^{i-1} (1 - p_j(u, v) \alpha_j), \quad (1)$$

where $I(u, v)$ represents the pixel color at the position (u, v) within the image plane; $p_i(u, v)$ denotes the 2D projection $\mathbf{x}_i^{2d} \sim \mathcal{N}(\boldsymbol{\mu}_i^{2d}, \boldsymbol{\Sigma}_i^{2d})$ of the i -th 3D Gaussian ellipsoid $\mathbf{x}_i \sim \mathcal{N}(\boldsymbol{\mu}_i, \boldsymbol{\Sigma}_i)$, indicating the probability density at pixel (u, v) , defined as $p_i(u, v) = p(u, v; \boldsymbol{\mu}_i^{2d}, \boldsymbol{\Sigma}_i^{2d})$; $c_i(d_i)$ indicates the color of the i -th visible Gaussian ellipsoid observed from the viewing direction d_i .

4D Gaussian Splatting (4DGS) [37] extends the Eq. (1) by introducing a timestamp t , thereby linking the color of each pixel not only with the spatial information of the projected 3D Gaussian \mathbf{x} but also with the temporal information. As a result, the pixel color representation in 3DGS, expressed as $\mathcal{I}(u, v)$, is extended to $\mathcal{I}(u, v, t)$, leading to:

$$\mathcal{I}(u, v, t) = \sum_{i=1}^N p_i(u, v, t) \alpha_i c_i(d) \prod_{j=1}^{i-1} (1 - p_j(u, v, t) \alpha_j), \quad (2)$$

where $p_i(u, v, t)$ denotes the probability density of the i -th projected 3D Gaussian ellipsoid at pixel (u, v) at the current time t . To model the Gaussian distribution that changes over time, 4DGS [37] introduces Gaussian parameter corrections based on temporal dependencies, defined as:

$$\boldsymbol{\mu}_t = \boldsymbol{\mu}_0 + \Delta\boldsymbol{\mu}_t, \boldsymbol{\Sigma}_t = \boldsymbol{\Sigma}_0 + \Delta\boldsymbol{\Sigma}_t, \quad (3)$$

where, $\boldsymbol{\mu}_0$ and $\boldsymbol{\Sigma}_0$ represent the original 3D Gaussian distribution within the canonical space, while $\Delta\boldsymbol{\mu}_t$ and $\Delta\boldsymbol{\Sigma}_t$ are dynamically adjusted according to the timestamp t using a

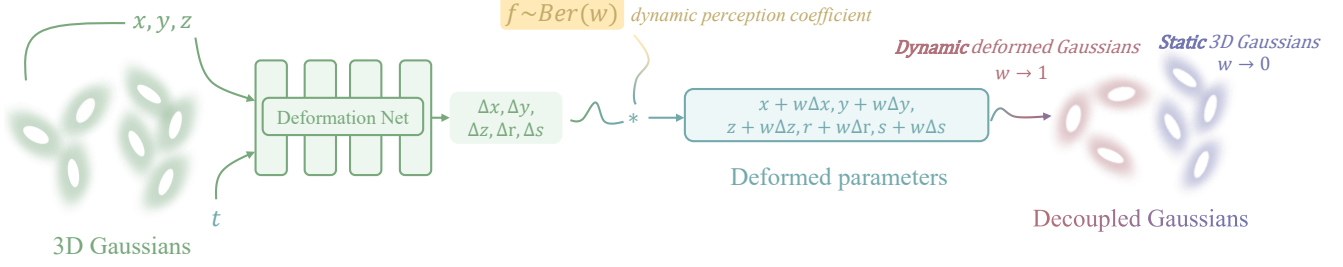


Figure 2. **Overview of the proposed SDD-4DGS pipeline for static-dynamic decoupling in 4D reconstruction.** The framework decouples static and dynamic components by integrating a novel dynamic perception coefficient into 4DGS [37]. The pipeline involves several key stages: initialization of 3D Gaussians, computation of deformation parameters through a deformation network, and dynamic regulation using the dynamic perception coefficient. Gaussians are then decoupled into static and dynamic groups, each optimized separately through loss functions which are detailed in Sec. 3.2.2.

spatio-temporal structure encoder and a multi-head Gaussian deformation decoder. Upon obtaining the deformed 3D Gaussian $\mathbf{x}_t \sim \mathcal{N}(\boldsymbol{\mu}_t, \boldsymbol{\Sigma}_t)$ at a given timestamp t , it projects the 3D Gaussian ellipsoid \mathbf{x}_t into a 2D Gaussian ellipsoid $\mathbf{x}_t^{2d} \sim \mathcal{N}(\boldsymbol{\mu}_t^{2d}, \boldsymbol{\Sigma}_t^{2d})$. Therefore, the term $p_i(u, v, t)$ in Eq. (2) can be denoted as:

$$p_i(u, v, t) = p(u, v; \boldsymbol{\mu}_{i,t}^{2d}, \boldsymbol{\Sigma}_{i,t}^{2d} | t) \cdot p(t), \quad (4)$$

where $p(t)$ denotes the time-dependent probability, and 4DGS [37] assigns it a default constant value of 1 to adapt to dynamic variations at different time points. Additional details can be found in 4DGS.

Overall, 4DGS merges spatial positioning with temporal information, primarily by incorporating the time variable t into a probabilistic model to represent dynamic variations, as in the Eq. (4). However, this approach neglects the intricate relationships that exist between dynamic and static scenes, lacking the necessary decoupling of dynamic and static attributes, which significantly complicates dynamic capture and modeling in complex scenarios.

3.2. Proposed Method: SDD-4DGS

To effectively identify and model the properties of dynamic and static components during 4D scene reconstruction, we propose a probabilistic dynamic perception-based decoupled Gaussian splatting method, as illustrated in Fig. 2. This framework achieves static-dynamic separation through the introduction of a dynamic perception coefficient. Below, we elaborate on our approach’s theoretical foundation (Sec. 3.2.1) and implementation considerations (Sec. 3.2.2).

3.2.1. Static-Dynamic aware Decoupling Framework

To decouple dynamic and static components within the scene during modeling, we propose the dynamic perception coefficient f in addition to the timestamp t for dynamic scene modeling [37]. The perception coefficient f can be regarded as a learnable parameter added to each Gaussian ellipsoid, which is jointly learned with other reconstruction parameters during optimization.

Specifically, we augment the rendering function in Eq. (4) by introducing a coefficient, enabling the deformed 3D Gaussian projection $p_i(u, v, t)$ to depend on both time t and a dynamic perception coefficient f :

$$p_i(u, v, t) = p(u, v; \boldsymbol{\mu}_{i,t}^{2d}, \boldsymbol{\Sigma}_{i,t}^{2d} | t, f_i) \cdot p(t, f_i), \quad (5)$$

where $p(t, f_i)$ denotes the joint probability distribution of time t and the dynamic perception coefficient f of i -th Gaussian ellipsoid. Considering the irrelevance between the inherent component properties and time, the joint probability distribution satisfies $p(t, f) = p(t) \cdot p(f)$. Further, based on the work [37], $p(t)$ is assumed to be a constant 1 for model simplification, thus Eq. (5) is simplified to:

$$p_i(u, v, t) = p(u, v; \boldsymbol{\mu}_{i,t}^{2d}, \boldsymbol{\Sigma}_{i,t}^{2d} | t, f_i) \cdot p(f_i). \quad (6)$$

Within a given time interval, each Gaussian ellipsoid only exist in only one of two mutually exclusive status, dynamic or static, with f_i adhering to a Bernoulli distribution, $f \sim \mathcal{B}(w)$, $p(f | w) = w^f(1-w)^{1-f}$, which means the i -th Gaussian ellipsoid is part of the dynamic scene when $f_i = 1$. Consequently, Eq. (6) is expressed as:

$$p(u, v; \boldsymbol{\mu}_{i,t}^{2d}, \boldsymbol{\Sigma}_{i,t}^{2d} | t, f_i) p(f_i) = \underbrace{p_i(u, v | t, f_i = 1)}_{\text{dynamic characteristic}} p(f_i = 1) + \underbrace{p_i(u, v | t, f_i = 0)}_{\text{static characteristic}} p(f_i = 0), \quad (7)$$

where $p_i(u, v | t, f_i = 1)$ and $p_i(u, v | t, f_i = 0)$ denote the dynamic and static characteristics of the Gaussian ellipsoid, respectively. Based on 4DGS [37], we characterize the Gaussian’s static attributes within the canonical space as $\mathbf{x}_0 \sim \mathcal{N}(\boldsymbol{\mu}_0, \boldsymbol{\Sigma}_0)$ and dynamic attributes as $\mathbf{x}_t \sim \mathcal{N}(\boldsymbol{\mu}_t, \boldsymbol{\Sigma}_t)$ in Eq. (3), and represent the deformed Gaussian $\mathbf{x}_t' \sim \mathcal{N}(\boldsymbol{\mu}_t', \boldsymbol{\Sigma}_t')$ in our framework using the following formulation:

$$\begin{aligned} \boldsymbol{\mu}_t' &= (1-w)\boldsymbol{\mu}_0 + w\boldsymbol{\mu}_t \\ &= (1-w)\boldsymbol{\mu}_0 + w(\boldsymbol{\mu}_0 + \Delta\boldsymbol{\mu}_t) \\ &= \boldsymbol{\mu}_0 + w\Delta\boldsymbol{\mu}_t, \\ \boldsymbol{\Sigma}_t' &= \boldsymbol{\Sigma}_0 + w\Delta\boldsymbol{\Sigma}_t. \end{aligned} \quad (8)$$

Additionally, by regularizing the probability density of the regulation factor f as follows:

$$\begin{aligned}\mathcal{L}_{bi} &= -p(f|w)\log(p(f|w)) \\ &= -(w\log(w) + (1-w)\log(1-w)).\end{aligned}\quad (9)$$

We guide $p(f)$ towards a single state, meaning each Gaussian ellipsoid possesses only one of the dynamic or static characteristics, further achieving separation of the dynamic component $\mathcal{G}_d = \{\boldsymbol{\mu}', \mathbf{S}', \mathbf{R}', c, \alpha, w \mid w > \tau_d\}$ and static component $\mathcal{G}_s = \{\boldsymbol{\mu}', \mathbf{S}', \mathbf{R}', c, \alpha, w \mid w < \tau_s\}$ of the reconstructed scene through dynamic threshold τ_t and static threshold τ_s filtering.

3.2.2. Implementation Optimization Strategy

Based on the theoretical derivation of the dynamic perception coefficient proposed in Sec. 3.2.1, each Gaussian’s dynamic properties can be regulated by the parameter w . This parameterization naturally integrates into existing Gaussian reconstruction pipelines enabling adaptive static-dynamic decoupling without requiring complex architectural modifications. However, to fully realize the potential of this theoretical framework, we must address two key implementation challenges.

First, while theoretically the dynamic perception coefficient should converge toward binary states, enforcing this constraint too early in training may degrade the final reconstruction quality, as shown in Tab. 4 (the experiments from (b) to (c) $-0.42dB$ PSNR). This occurs because during early training, scene geometry and appearance features have not yet converged, and forcing coefficient binarization may prematurely restrict the model’s expressive capacity. To address this issue, we implement a *progressive constraint schedule* through a weighting function

$$\lambda_{bi}(t) = 1 - e^{-\alpha t} \quad (10)$$

, where α controls the rate at which binary constraints are applied. This progressive schedule allows the model to first establish fundamental scene geometry before enforcing strict dynamic-static separation.

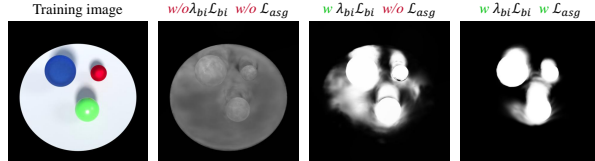


Figure 3. **Visualization of optimization strategy effects on dynamic perception coefficient.** From left to right: training image, results without binary constraint and self-supervision (w/o $\lambda_{bi}\mathcal{L}_{bi}$ w/o \mathcal{L}_{asg}), with only binary constraint (w $\lambda_{bi}\mathcal{L}_{bi}$ w/o \mathcal{L}_{asg}), and with both binary constraint and self-supervision (w $\lambda_{bi}\mathcal{L}_{bi}$ w \mathcal{L}_{asg}). The introduction of self-supervision signals significantly improves static-dynamic decoupling.

Second, the core objective of the dynamic perception coefficient is to achieve physically meaningful scene decoupling. However, when optimized solely with reconstruction loss, the model may converge to local optima where stationary backgrounds are incorrectly classified as dynamic regions or slowly moving objects are misidentified as static structures (Fig. 3)—errors that directly degrade rendering quality. To address this, we introduce a simple yet effective *automatic supervision signal*. Drawing on the widely observed phenomenon that “dynamic regions typically exhibit higher uncertainty during reconstruction,” we incorporate a lightweight uncertainty estimation mechanism [16] to generate motion masks m , enabling end-to-end optimization:

$$\begin{aligned}\mathcal{L}_{asg} &= (1-m)(\mathcal{L}_1(\hat{I}_s, I) + \mathcal{L}_{ssim}(\hat{I}_s, I)) \\ &\quad + m(\mathcal{L}_1(\hat{I}_d, I) + \mathcal{L}_{ssim}(\hat{I}_d, I))\end{aligned}\quad (11)$$

, where \hat{I}_d and \hat{I}_s represent the renderings from the dynamic part \mathcal{G}_d and static part \mathcal{G}_s of the scene, respectively. More implementation details are provided in the supplementary materials.

3.3. Training Objective

Our SDD-4DGS framework incorporates a dynamic perception coefficient for effective static-dynamic decoupling. The complete optimization objective consists of three key components:

$$\mathcal{L} = \mathcal{L}_{4dgs} + \lambda_{bi}(t)\mathcal{L}_{bi} + \mathcal{L}_{asg} \quad (12)$$

, where \mathcal{L}_{4dgs} represents the fundamental 4DGS reconstruction loss from [37], encompassing rendering fidelity and regularization terms; \mathcal{L}_{bi} denotes the binary entropy loss (Eq. (9)) that constrains the static-dynamic attributes of each Gaussian to converge toward a single state; and \mathcal{L}_{asg} is the automatic supervision guidance loss (Eq. (11)) that optimizes dynamic and static regions separately based on uncertainty estimation.

4. Experiment

In this section, we first detail our implementation and hyperparameter setting in Sec. 4.1. Then, Sec. 4.2 compares our method’s performance against other methods on the five datasets under four distinct setting. Finally, Sec. 4.3 provides ablation results, demonstrating the rationale of each module’s design.

4.1. Implementation & Hyperparameter Setting

We develop our method based on the PyTorch [30] framework, conducting all experiments on a single RTX 3090 GPU. Specifically, we use the Adam optimizer and trained for 30,000 steps across all datasets.

We carefully select hyperparameters to balance theoretical alignment with practical performance. For the dynamic perception coefficient thresholds, we empirically determine

Table 1. **Quantitative results on the monocular real datasets Nerfies [28] and HyperNeRF [29].** The best results are highlighted in bold. The rendering resolution is set to 960×540 .

HyperNeRF	Broom		3D Printer		Chicken		Peel Banana	
	PSNR (dB) \uparrow	SSIM \uparrow	PSNR (dB) \uparrow	SSIM \uparrow	PSNR (dB) \uparrow	SSIM \uparrow	PSNR (dB) \uparrow	SSIM \uparrow
4DGS [37]	22.40	0.641	24.55	0.813	23.81	0.857	22.33	0.765
RealTime4DGS [43]	21.25	0.560	18.04	0.581	20.00	0.642	21.14	0.649
Spacetime [19]	21.74	0.606	22.51	0.753	21.16	0.793	21.72	0.737
4DRotor [6]	20.98	0.554	18.44	0.630	19.09	0.694	20.09	0.657
SDD-4DGS (Ours)	23.16	0.673	24.76	0.818	24.67	0.873	22.62	0.772

Nerfies	Curis		Tail		Toby-sit		Mean		
	PSNR (dB) \uparrow	SSIM \uparrow	PSNR (dB) \uparrow	SSIM \uparrow	PSNR (dB) \uparrow	SSIM \uparrow	PSNR (dB) \uparrow	SSIM \uparrow	FPS \uparrow
4DGS [37]	15.11	0.561	26.82	0.717	21.45	0.539	22.35	0.699	60.2
RealTime4DGS [43]	17.68	0.499	23.53	0.555	19.87	0.384	20.21	0.553	72.1
Spacetime [19]	20.26	0.670	25.40	0.650	21.31	0.451	22.01	0.665	70.2
4DRotor [6]	15.50	0.546	19.89	0.477	19.50	0.373	19.07	0.562	38.4
SDD-4DGS (Ours)	20.14	0.670	26.67	0.725	21.23	0.578	23.32	0.730	62.3

$\tau_d = \tau_s = 0.5$ during training to ensure smoother optimization, These thresholds optimally separate the emerging bimodal distribution while maintaining reconstruction stability (Fig. 4.). During inference, we tighten these thresholds to $\tau_d = 0.85$ and $\tau_s = 0.2$ to ensure precise component classification after full convergence. The progressive constraint schedule ($\lambda_{bi}(t) = 1 - e^{-\alpha t}$) represents a critical implementation choice. After extensive experimentation, we set $\alpha = 1 \times 10^{-4}$, which creates an optimal trajectory that allows geometry and appearance to stabilize before enforcing strict dynamic-static classification. Other parameters, including learning rate, densification, pruning, and opacity reset, are set following prior work [14]. Further implementation details can be found in the supplementary materials.

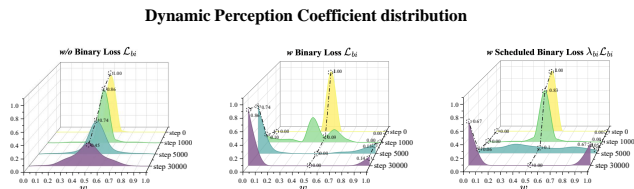


Figure 4. **Visualization of the dynamic perception coefficient distribution over training steps.**

4.2. Comparison with SOTA

Evaluation on Monocular Real-world Scene. Monocular scene reconstruction faces challenges of sparse viewpoints and spatiotemporal imbalances between dynamic and static scene distributions. We test SDD-4DGS and all baselines on HyperNeRF [29] and Nerfies [28]. SDD-4DGS achieves state-of-the-art results in 5 out of 7 scenes (Tab. 1) and improves reconstruction of dynamic textures and high-frequency details (Fig 5) in all scenes. Furthermore, we independently render dynamic and static scenes for analysis. SDD-4DGS accurately captures static structures and dynamic movements like printer heads and hand motions.

This reduces scene ambiguity, captures static details thoroughly, and integrates dynamic/static information, mitigating issues from viewpoint shifts and sparse observations.

Table 2. **Quantitative results on the multi-view real dataset Neu3D’s [17].** The best results are highlighted in bold. The rendering resolution is set to 1352×1014 .

Method	PSNR (dB) \uparrow	SSIM \uparrow	LPIPS \downarrow
K-Planes [7]	31.63	-	-
MixVoxels-X [36]	31.73	-	0.06
4DGS [37]	31.23	0.93	0.12
RealTime4DGS [43]	31.84	0.95	0.09
Spacetime [19]	31.38	0.94	0.12
4DRotor [6]	31.73	0.94	0.10
SDD-4DGS (Ours)	32.39	0.95	0.09

Evaluation on Multi-view Real-world Scene. As shown in Tab. 2, SDD-4DGS achieves an average PSNR of 32.39dB in Neu3D’s [17] dataset, which exceeds the prior best of 31.84dB. In Fig. 7, we illustrate the rendering performance and depth of some methods. Most methods achieve satisfactory rendering quality with the scene details captured by multi-view cameras. However, our method demonstrates superior detail in certain aspects, such as objects outside windows, fabric folds, and color rendering of semi-transparent materials. Additionally, in terms of geometric modeling, SDD-4DGS effectively distinguishes foreground from background and achieves enhanced local consistency in depth representation.

To further examine the spatial distribution of points, we provide a visualization in Fig 6. As observed, our method demonstrates a more focused distribution of points in the dynamic regions, particularly in contrast to 4DGS [37] and Spacetime [19], where the distribution is affected by static components within the dynamic sections.

Evaluation on Monocular Synthetic Scene. As a key benchmark for assessing 4D dynamic scene reconstruction, the monocular synthetic dataset D-NeRF [31] measures the

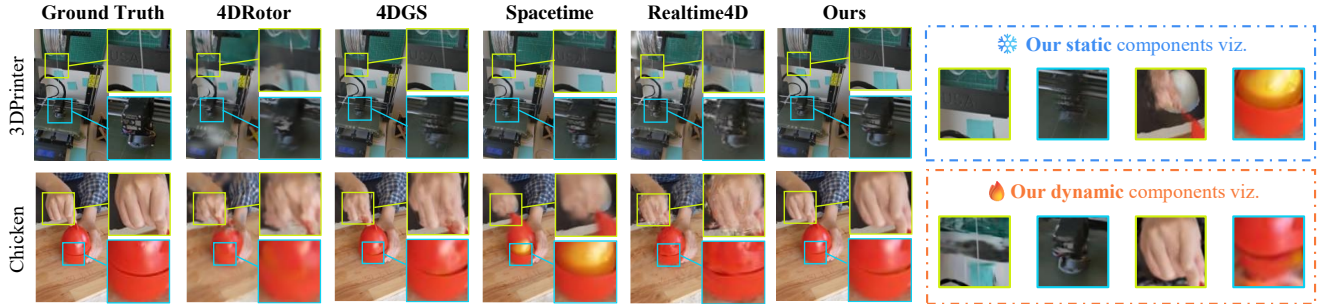


Figure 5. **Qualitative comparison between rendered results of HyperNeRF [29] dataset.** We visualize the rendering results of our method with those of other methods [6, 19, 37, 43] and enlarge the local details. In addition, in order to more intuitively demonstrate our separation effect, we render the static and dynamic scenes mentioned in the method separately.

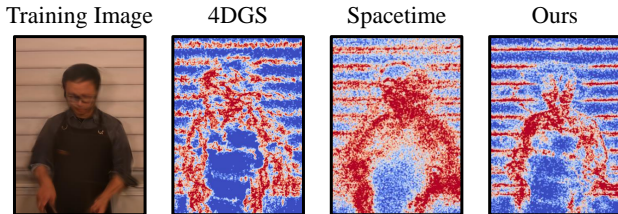


Figure 6. **Visualization of point distribution in dynamic regions.** The point density across regions illustrates the distinct spatial distribution achieved by our SDD-4DGS framework in separating static and dynamic components. Compared to prior methods (e.g., 4DGS [37] and Spacetime [19]), our approach demonstrates a more concentrated point allocation which reflects the effectiveness of the proposed decoupling mechanism, reducing static-dynamic interference.

foundational capabilities of different methods in constructing dynamic scenes. To thoroughly evaluate the rendering quality of both dynamic and static components, we manually segmented the dynamic regions within the images, as illustrated in Fig 1(a). We computed the PSNR values for the static regions, dynamic regions, and the overall image separately in Tab. 3. Experimental results demonstrate that, due to our decoupling and optimization strategies, SDD-4DGS achieves improved reconstruction quality across both static and dynamic areas, highlighting the critical role of decoupled modeling in enhancing rendering performance.

Urban Scene Evaluation. High-speed vehicle traffic in urban environments challenges 4D reconstruction methodologies. Our approach employs targeted supervision for dynamic regions during training, enhancing dynamic capture. Fig. 8 shows sampled points and their tracking signals, highlighting our method’s superior motion modeling for fast-moving objects over 4DGS [37]. Quantitative results are detailed in the supplementary materials.

4.3. Ablation Studies

Table 4 demonstrates the impact of our method’s core components on reconstruction performance using the D-

Table 3. **Quantitative results on the synthesis dataset D-NeRF [31].** The best results are highlighted in bold. The rendering resolution is set to 800×800 .

PSNR (dB)↑	Trex			Jumping Jacks		
	static	dynamic	full	static	dynamic	full
4DGS [37]	25.31	20.32	25.08	34.74	25.49	34.51
RealTime4DGS [43]	25.44	19.93	24.71	29.65	21.13	29.45
Spacetime [19]	24.86	19.78	24.67	30.85	22.36	30.62
4DRotor [6]	25.46	22.37	25.27	29.99	25.86	29.92
SDD-4DGS (Ours)	25.36	23.38	25.31	35.79	26.98	35.58

PSNR (dB)↑	Mutant			Mean		
	static	dynamic	full	static	dynamic	full
4DGS [37]	39.53	24.02	36.85	32.19	23.27	32.14
RealTime4DGS [43]	33.55	22.65	32.43	29.54	21.23	28.86
Spacetime [19]	34.94	24.97	32.82	30.21	22.37	29.37
4DRotor [6]	39.44	27.85	38.15	31.63	25.36	31.11
SDD-4DGS (Ours)	40.35	27.42	38.67	33.83	25.92	33.18

NeRF [31] dataset. We systematically evaluated our implementation strategies through controlled experiments to analyze the effects of progressive binary constraint and automatic supervision signals.

Dynamic Perception Coefficient Analysis: Our baseline configuration (Tab. 4 (a)) represents the standard 4D Gaussian Splatting approach [37] without our proposed components, achieving a PSNR of 34.14dB. Introducing the dynamic perception coefficient w (Tab. 4 (b)) yields a notable improvement to 34.34dB PSNR and 0.95 SSIM. This improvement validates our theoretical assertion that explicitly modeling the static-dynamic nature of scene components through a probabilistic framework enhances reconstruction fidelity.

Effect of Progressive Binary Constraint: Tab. 4 (c) shows that introducing binary entropy loss (\mathcal{L}_{bi}) without progressive weight scheduling (λ_{bi}) results in a PSNR decrease. However, when the progressive weight scheduling mechanism is incorporated (Tab. 4 (c)), performance significantly improves to 34.63dB. This confirms our argument in Section 3.2.2 that enforcing binarization too early restricts model expressivity, while progressive constraint introduction effectively balances reconstruction quality and static-dynamic separation.

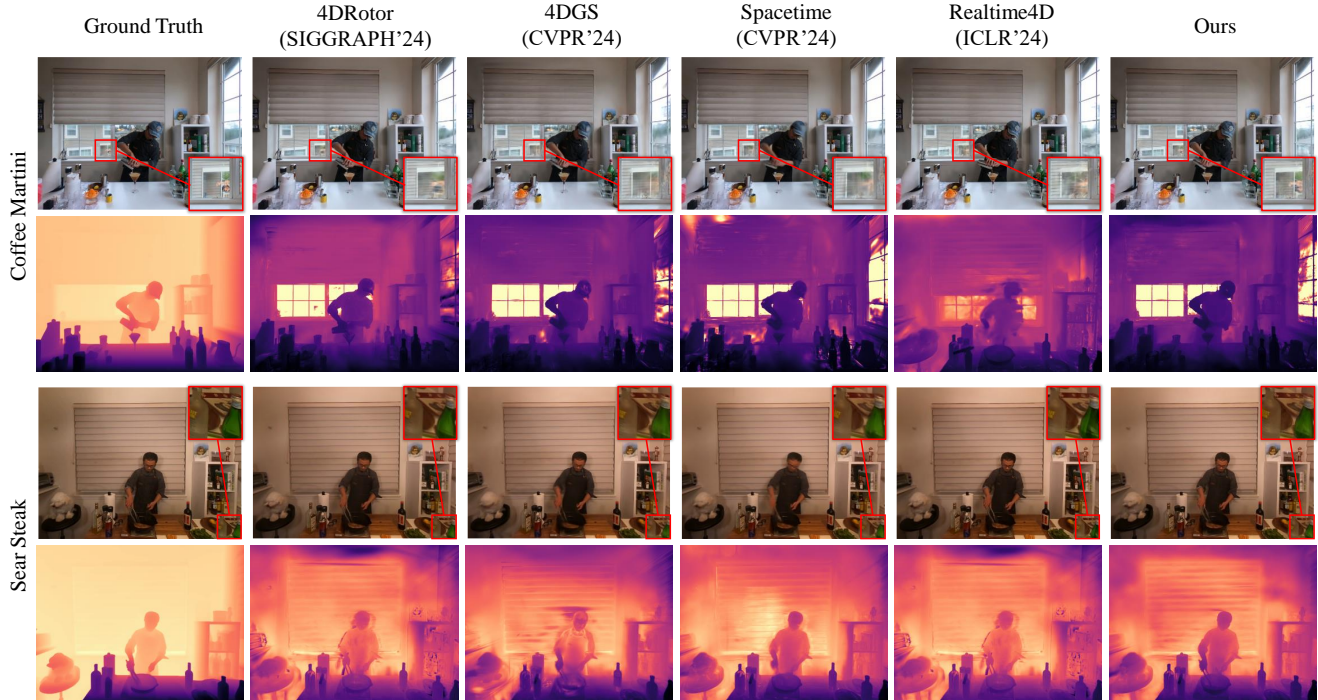


Figure 7. **Qualitative comparison between rendered results of Neu3D’s [17] dataset.** We visualize the rendering results of our method with those of other methods [6, 19, 37, 43] and enlarge the local details. Additionally, we rendered the depth map of the scene. The ground truth depth map, estimated by method [42], serves as a reference for comparison. Compared with other methods, the local brightness in our depth map is more consistent.

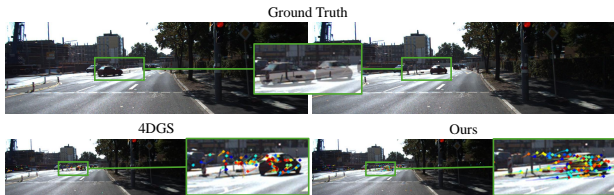


Figure 8. **Visualization of tracking with 3D Gaussians.** We superimpose local pictures of the ground truth to show the real motion situation and visualize the motion trajectory of the 3D Gaussians predicted by 4DGS [37] and our method.

Contribution of Automatic Supervision: The experiments from (d) to (Full) in Tab. 4 demonstrate the value of automatic supervision signals. When introducing the explicit loss \mathcal{L}_{asg} , PSNR improves by 0.19dB, and it enables the model to achieve optimal performance. This progression confirms that automatic supervision signals effectively address local optima issues in dynamic-static classification, particularly in correctly separating complex scenes.

5. Conclusion

We propose SDD-4DGS, an innovative framework for 4D scene reconstruction that employs static-dynamic aware decoupling within Gaussian Splatting. Our method incorporates a probabilistic formulation of dynamic perception

Table 4. **Ablation study on the D-NeRF dataset.** The baseline (a) represents standard 4DGS [37]. The dynamic perception coefficient w (b) and the combination of binary entropy loss \mathcal{L}_{bi} with progressive scheduling ($\lambda_{bi}L_{bi}$) (d) improve performance. The *Full* model, which includes automatic supervision signals \mathcal{L}_{asg} , achieves optimal results, highlighting the effectiveness of our static-dynamic aware decoupling framework.

ID	Ablation Items				D-NeRF	
	w	\mathcal{L}_{bi}	λ_{bi}	\mathcal{L}_{asg}	PSNR (dB)↑	SSIM↑
a					34.14	0.94
b	✓				34.34	0.95
c	✓	✓			33.92	0.94
d	✓	✓	✓		34.63	0.95
Full	✓	✓	✓	✓	34.82	0.96

into the Gaussian reconstruction pipeline. With optimized strategies, we leverage this framework in practical applications. Evaluations on various datasets show our approach outperforms existing techniques, reducing scene ambiguity and static-dynamic interference. This framework provides a robust solution for real-world 4D reconstructions, with potential for future research in complex scenarios like dynamic lighting and deformable objects, as well as integration with neural rendering for real-time use.

References

- [1] Mario Alfonso-Arsuaga, Jorge García-González, Andrea Castiella-Aguirrezabala, Miguel Andrés Alonso, and Elena Garcés. Dynrfactor: Temporally consistent intrinsic scene decomposition for dynamic nerfs. *Computers & Graphics*, 122:103984, 2024. 3
- [2] Ang Cao and Justin Johnson. Hexplane: A fast representation for dynamic scenes. In *Proceedings of the IEEE/CVF Conference on Computer Vision and Pattern Recognition*, pages 130–141, 2023. 3
- [3] Quei-An Chen and Akihiro Tsukada. Flow supervised neural radiance fields for static-dynamic decomposition. In *2022 International Conference on Robotics and Automation (ICRA)*, pages 10641–10647. IEEE, 2022. 3
- [4] Marius Cordts, Mohamed Omran, Sebastian Ramos, Timo Rehfeld, Markus Enzweiler, Rodrigo Benenson, Uwe Franke, Stefan Roth, and Bernt Schiele. The cityscapes dataset for semantic urban scene understanding. In *Proceedings of the IEEE conference on computer vision and pattern recognition*, pages 3213–3223, 2016. 1
- [5] Wei Dong, Jieqi Shi, Weijie Tang, Xin Wang, and Hongbin Zha. An efficient volumetric mesh representation for real-time scene reconstruction using spatial hashing. In *2018 IEEE International Conference on Robotics and Automation (ICRA)*, pages 6323–6330. IEEE, 2018. 3
- [6] Yuanxing Duan, Fangyin Wei, Qiyu Dai, Yuhang He, Wenzheng Chen, and Baoquan Chen. 4d-rotor gaussian splatting: towards efficient novel view synthesis for dynamic scenes. In *ACM SIGGRAPH 2024 Conference Papers*, pages 1–11, 2024. 1, 3, 6, 7, 8, 2
- [7] Sara Fridovich-Keil, Giacomo Meanti, Frederik Rahbæk Warburg, Benjamin Recht, and Angjoo Kanazawa. K-planes: Explicit radiance fields in space, time, and appearance. In *Proceedings of the IEEE/CVF Conference on Computer Vision and Pattern Recognition*, pages 12479–12488, 2023. 6, 2
- [8] Wanshui Gan, Hongbin Xu, Yi Huang, Shifeng Chen, and Naoto Yokoya. V4d: Voxel for 4d novel view synthesis. *IEEE Transactions on Visualization and Computer Graphics*, 2023. 2
- [9] Chen Gao, Ayush Saraf, Johannes Kopf, and Jia-Bin Huang. Dynamic view synthesis from dynamic monocular video. In *Proceedings of the IEEE/CVF International Conference on Computer Vision*, pages 5712–5721, 2021. 3
- [10] Paulo FU Gotardo, Tomas Simon, Yaser Sheikh, and Iain Matthews. Photogeometric scene flow for high-detail dynamic 3d reconstruction. In *Proceedings of the IEEE international conference on computer vision*, pages 846–854, 2015. 3
- [11] Shengyu Huang, Zan Gojcic, Jiahui Huang, Andreas Wieser, and Konrad Schindler. Dynamic 3d scene analysis by point cloud accumulation. In *European Conference on Computer Vision*, pages 674–690. Springer, 2022. 3
- [12] Anupama K Ingale et al. Real-time 3d reconstruction techniques applied in dynamic scenes: A systematic literature review. *Computer Science Review*, 39:100338, 2021. 1
- [13] Pushyami Kaveti, Sammie Katt, and Hanumant Singh. Removing dynamic objects for static scene reconstruction using light fields. *arXiv preprint arXiv:2003.11076*, 2020. 3
- [14] Bernhard Kerbl, Georgios Kopanas, Thomas Leimkühler, and George Drettakis. 3d gaussian splatting for real-time radiance field rendering. *ACM Trans. Graph.*, 42(4):139–1, 2023. 1, 2, 3, 6
- [15] Hansung Kim, Jean-Yves Guillemaut, Takeshi Takai, Muhammad Sarim, and Adrian Hilton. Outdoor dynamic 3d scene reconstruction. *IEEE Transactions on Circuits and Systems for Video Technology*, 22(11):1611–1622, 2012. 3
- [16] Jonas Kulhanek, Songyou Peng, Zuzana Kukelova, Marc Pollefeys, and Torsten Sattler. Wildgaussians: 3d gaussian splatting in the wild. *arXiv preprint arXiv:2407.08447*, 2024. 3, 5, 4
- [17] Tianye Li, Mira Slavcheva, Michael Zollhoefer, Simon Green, Christoph Lassner, Changil Kim, Tanner Schmidt, Steven Lovegrove, Michael Goesele, Richard Newcombe, et al. Neural 3d video synthesis from multi-view video. In *Proceedings of the IEEE/CVF Conference on Computer Vision and Pattern Recognition*, pages 5521–5531, 2022. 3, 6, 8, 1, 2
- [18] Zhengqi Li, Simon Niklaus, Noah Snavely, and Oliver Wang. Neural scene flow fields for space-time view synthesis of dynamic scenes. In *Proceedings of the IEEE/CVF Conference on Computer Vision and Pattern Recognition*, pages 6498–6508, 2021. 3
- [19] Zhan Li, Zhang Chen, Zhong Li, and Yi Xu. Spacetime gaussian feature splatting for real-time dynamic view synthesis. In *Proceedings of the IEEE/CVF Conference on Computer Vision and Pattern Recognition*, pages 8508–8520, 2024. 1, 3, 6, 7, 8, 2
- [20] Lingjie Liu, Jiatao Gu, Kyaw Zaw Lin, Tat-Seng Chua, and Christian Theobalt. Neural sparse voxel fields. *Advances in Neural Information Processing Systems*, 33:15651–15663, 2020. 3
- [21] Xingyu Liu, Mengyuan Yan, and Jeannette Bohg. Meteor-net: Deep learning on dynamic 3d point cloud sequences. In *Proceedings of the IEEE/CVF International Conference on Computer Vision*, pages 9246–9255, 2019. 3
- [22] Yu-Lun Liu, Chen Gao, Andreas Meuleman, Hung-Yu Tseng, Ayush Saraf, Changil Kim, Yung-Yu Chuang, Johannes Kopf, and Jia-Bin Huang. Robust dynamic radiance fields. In *Proceedings of the IEEE/CVF Conference on Computer Vision and Pattern Recognition*, pages 13–23, 2023. 3
- [23] Yujie Lu, Shuo Wang, Sensen Fan, Jiahui Lu, Peixian Li, and Pingbo Tang. Image-based 3d reconstruction for multi-scale civil and infrastructure projects: A review from 2012 to 2022 with new perspective from deep learning methods. *Advanced Engineering Informatics*, 59:102268, 2024. 1
- [24] Moritz Menze and Andreas Geiger. Object scene flow for autonomous vehicles. In *Proceedings of the IEEE conference on computer vision and pattern recognition*, pages 3061–3070, 2015. 3, 1, 2, 4
- [25] Ben Mildenhall, Pratul P Srinivasan, Matthew Tancik, Jonathan T Barron, Ravi Ramamoorthi, and Ren Ng. Nerf: Representing scenes as neural radiance fields for view syn-

- thesis. *Communications of the ACM*, 65(1):99–106, 2021. [3](#)
- [26] Maxime Oquab, Timothée Darcet, Théo Moutakanni, Huy Vo, Marc Szafraniec, Vasil Khalidov, Pierre Fernandez, Daniel Haziza, Francisco Massa, Alaaeldin El-Nouby, et al. Dinov2: Learning robust visual features without supervision. *arXiv preprint arXiv:2304.07193*, 2023. [3](#), [4](#)
- [27] Julian Ost, Fahim Mannan, Nils Thuerey, Julian Knodt, and Felix Heide. Neural scene graphs for dynamic scenes. In *Proceedings of the IEEE/CVF Conference on Computer Vision and Pattern Recognition*, pages 2856–2865, 2021. [3](#)
- [28] Keunhong Park, Utkarsh Sinha, Jonathan T Barron, Sofien Bouaziz, Dan B Goldman, Steven M Seitz, and Ricardo Martin-Brualla. Nerfies: Deformable neural radiance fields. In *Proceedings of the IEEE/CVF International Conference on Computer Vision*, pages 5865–5874, 2021. [3](#), [6](#), [1](#)
- [29] Keunhong Park, Utkarsh Sinha, Peter Hedman, Jonathan T Barron, Sofien Bouaziz, Dan B Goldman, Ricardo Martin-Brualla, and Steven M Seitz. Hypernerf: A higher-dimensional representation for topologically varying neural radiance fields. *arXiv preprint arXiv:2106.13228*, 2021. [3](#), [6](#), [7](#), [1](#)
- [30] Adam Paszke, Sam Gross, Francisco Massa, Adam Lerer, James Bradbury, Gregory Chanan, Trevor Killeen, Zeming Lin, Natalia Gimelshein, Luca Antiga, et al. Pytorch: An imperative style, high-performance deep learning library. *Advances in neural information processing systems*, 32, 2019. [5](#)
- [31] Albert Pumarola, Enric Corona, Gerard Pons-Moll, and Francesc Moreno-Noguer. D-nerf: Neural radiance fields for dynamic scenes. In *Proceedings of the IEEE/CVF Conference on Computer Vision and Pattern Recognition*, pages 10318–10327, 2021. [3](#), [6](#), [7](#), [1](#), [2](#)
- [32] Weining Ren, Zihan Zhu, Boyang Sun, Jiaqi Chen, Marc Pollefeys, and Songyou Peng. Nerf on-the-go: Exploiting uncertainty for distractor-free nerfs in the wild. In *Proceedings of the IEEE/CVF Conference on Computer Vision and Pattern Recognition*, pages 8931–8940, 2024. [3](#)
- [33] Viktor Rudnev, Mohamed Elgharib, William Smith, Lingjie Liu, Vladislav Golyanik, and Christian Theobalt. Nerf for outdoor scene relighting. In *European Conference on Computer Vision*, pages 615–631. Springer, 2022. [3](#)
- [34] Ayush Tewari, Justus Thies, Ben Mildenhall, Pratul Srinivasan, Edgar Tretschk, Wang Yifan, Christoph Lassner, Vincent Sitzmann, Ricardo Martin-Brualla, Stephen Lombardi, et al. Advances in neural rendering. In *Computer Graphics Forum*, pages 703–735. Wiley Online Library, 2022. [1](#)
- [35] Vadim Tschernezki, Diane Larlus, and Andrea Vedaldi. Neuraldiff: Segmenting 3d objects that move in egocentric videos. In *2021 International Conference on 3D Vision (3DV)*, pages 910–919. IEEE, 2021. [3](#)
- [36] Feng Wang, Sinan Tan, Xinghang Li, Zeyue Tian, Yafei Song, and Huaping Liu. Mixed neural voxels for fast multi-view video synthesis. In *Proceedings of the IEEE/CVF International Conference on Computer Vision*, pages 19706–19716, 2023. [6](#)
- [37] Guanjun Wu, Taoran Yi, Jiemin Fang, Lingxi Xie, Xiaopeng Zhang, Wei Wei, Wenyu Liu, Qi Tian, and Xinggang Wang. 4d gaussian splatting for real-time dynamic scene rendering. In *Proceedings of the IEEE/CVF Conference on Computer Vision and Pattern Recognition*, pages 20310–20320, 2024. [1](#), [2](#), [3](#), [4](#), [5](#), [6](#), [7](#), [8](#)
- [38] Tianhao Wu, Fangcheng Zhong, Andrea Tagliasacchi, Forrester Cole, and Cengiz Oztireli. D²nerf: Self-supervised decoupling of dynamic and static objects from a monocular video. *Advances in neural information processing systems*, 35:32653–32666, 2022. [1](#), [3](#)
- [39] Xiaolong Xie, Xusheng Guo, Wei Li, Jie Liu, and Jianfeng Xu. Deform2nerf: Non-rigid deformation and 2d–3d feature fusion with cross-attention for dynamic human reconstruction. *Electronics*, 12(21):4382, 2023. [3](#)
- [40] Zhiwen Yan, Chen Li, and Gim Hee Lee. Nerf-ds: Neural radiance fields for dynamic specular objects. In *Proceedings of the IEEE/CVF Conference on Computer Vision and Pattern Recognition*, pages 8285–8295, 2023. [3](#)
- [41] Gengshan Yang, Shuo Yang, John Z Zhang, Zachary Manchester, and Deva Ramanan. Ppr: Physically plausible reconstruction from monocular videos. In *Proceedings of the IEEE/CVF International Conference on Computer Vision*, pages 3914–3924, 2023. [3](#)
- [42] Lihe Yang, Bingyi Kang, Zilong Huang, Zhen Zhao, Xiaogang Xu, Jiashi Feng, and Hengshuang Zhao. Depth anything v2. *arXiv preprint arXiv:2406.09414*, 2024. [8](#)
- [43] Zeyu Yang, Hongye Yang, Zijie Pan, and Li Zhang. Real-time photorealistic dynamic scene representation and rendering with 4d gaussian splatting. *arXiv preprint arXiv:2310.10642*, 2023. [1](#), [3](#), [6](#), [7](#), [8](#), [2](#)
- [44] Raza Yunus, Jan Eric Lenssen, Michael Niemeyer, Yiyi Liao, Christian Ruppert, Christian Theobalt, Gerard Pons-Moll, Jia-Bin Huang, Vladislav Golyanik, and Eddy Ilg. Recent trends in 3d reconstruction of general non-rigid scenes. In *Computer Graphics Forum*, page e15062. Wiley Online Library, 2024. [1](#)
- [45] Chiyuan Zhang, Samy Bengio, Moritz Hardt, Benjamin Recht, and Oriol Vinyals. Understanding deep learning (still) requires rethinking generalization. *Communications of the ACM*, 64(3):107–115, 2021. [1](#)
- [46] Hao Zhang and Feng Xu. Mixedfusion: Real-time reconstruction of an indoor scene with dynamic objects. *IEEE transactions on visualization and computer graphics*, 24(12):3137–3146, 2017. [3](#)
- [47] Chengxuan Zhu, Renjie Wan, Yunkai Tang, and Boxin Shi. Occlusion-free scene recovery via neural radiance fields. In *Proceedings of the IEEE/CVF Conference on Computer Vision and Pattern Recognition*, pages 20722–20731, 2023. [3](#)

SDD-4DGS: Static-Dynamic Aware Decoupling in Gaussian Splatting for 4D Scene Reconstruction

Supplementary Material

6. Dataset Description

This section primarily presents detailed information about the selected datasets, which are categorized into four different types: monocular synthetic datasets (D-NeRF [31]), monocular real datasets (HyperNeRF [29] & Nerfies [28]), multi-view real datasets (Neu3D’s [17]), and real street scene datasets (KITTI [24]). Detailed dataset information can be found in Tab. 5, followed by descriptions of the data partitioning and related explanations.

D-NeRF [31] dataset comprises 8 scenes, with default training and testing splits. The highest resolution of 800×800 is selected for rendering comparisons.

HyperNeRF [29] dataset contains scenes from 14 monocular cameras and 4 binocular cameras. We select the four binocular scenes (*vrig-peel-banana*, *vrig-chicken*, *vrig-3dprinter*, *broom2*) for novel view synthesis. One camera is used for training and another for validation. We downsample to a resolution of 960×540 for rendering and initialize the point cloud using COLMAP.

Nerfies [28] dataset includes 4 binocular scenes, with “*broom*” being very similar to “*broom2*” in HyperNerf dataset. Therefore, we select three scenes (*curls*, *tail toby-sit*) for experiments. Similarly to the HyperNerf setup, we designate one camera for training and use the remaining camera for validation. We downsample to a resolution of 960×540 for rendering and initialize the point cloud using COLMAP.

Neu3D’s [17] dataset includes six multi-view scenes captured with 20 high-definition cameras in an indoor kitchen. We select five frequently used scenes for comparison (excluding *flame_salmon*). The original 2K video is downsampled to 1352×1014 for rendering, and we use the provided point clouds for initialization in all baseline comparisons.

KITTI [24] dataset contains 400 dynamic scenes from the KITTI raw data and we selected 5 scenes with 40 frames

Table 5. **Dataset overview used in the analysis.** The table lists the number of scenes, the presence of point clouds, and rendering resolutions. Further details on data partitioning are discussed in the following sections.

Datasets	Camera View	Scene Category	Scenes Num.	Initial Point Cloud	Resolution
D-NeRF [31]	Monocular	Synthetic	8	-	800×800
HyperNeRF [29]	Monocular	Outdoor	4	COLMAP	960×540
Nerfies [28]	Monocular	Outdoor	4	COLMAP	960×540
Neu3D’S [17]	Multi-view	Indoor	5	COLMAP	1352×1014
KITTI [24]	Monocular	Urban	7	COLMAP	1242×375

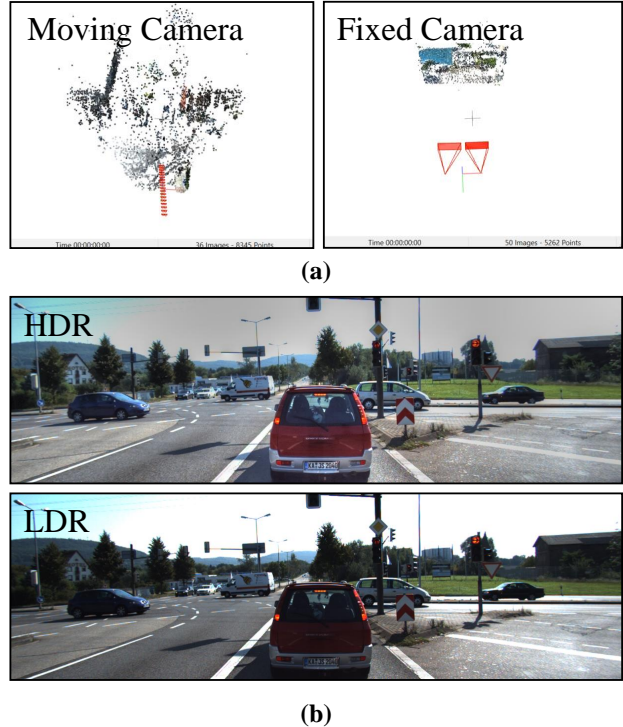


Figure 9. (a) Visualization of sparse point clouds initialized using COLMAP for fixed and moving cameras respectively, with the red triangular pyramid representing camera poses. (b) Comparison between Low Dynamic Range (LDR) and High Dynamic Range (HDR) image processed by *Photomatix*, showcasing the variation in scene illumination and tone mapping.

(20 from each camera) per scene for dataset construction. One viewpoint is used for training, while the other serves as validation. The five scenes include two captured from fixed cameras (parked) and three from moving cameras (in transit), as shown in Fig. 9 (a). Furthermore, we observed that in autonomous driving scenarios, low dynamic range (LDR) images captured due to direct sunlight significantly increase the difficulty of scene reconstruction. To mitigate this issue, we applied high dynamic range (HDR) processing to the images in one of the scenes using *Photomatix*¹, serving as a reference for reconstruction in autonomous driving scenarios that utilize high dynamic range images, as shown in Fig. 9 (b). All scenes are selected at the maximum resolution corresponding to the Ground Truth, with sparse point clouds initialized using COLMAP.

¹Photomatix: <https://www.hdrsoft.com/>

Table 6. **Quantitative results on the synthesis dataset D-NeRF [31].** The best results are highlighted in bold. The rendering resolution is set to 800×800 .

Method	# Volume	PSNR (dB)↑	SSIM ↑	LPIPS ↓	FPS ↑	Training Time (min) ↓
K-Planes [7]	CVPR'23	32.61	0.97	-	0.97	52.0
V4D [8]	TVCG'23	33.72	0.98	0.02	2.08	414.
4DGS [37]	CVPR'24	34.14	0.94	0.02	84.4	40.2
RealTime4DGS [43]	ICLR'24	30.55	0.94	0.06	100.	37.1
Spacetime [19]	CVPR'24	29.76	0.95	0.04	113.	10.0
4DRotor [6]	SIGGRAPH'24	31.73	0.97	0.03	47.2	102.
SDD-4DGS (Ours)	-	34.82	0.96	0.03	85.3	46.1



Figure 10. **Qualitative comparison between rendered results of D-NeRF [31] dataset.** We visualize the rendering results of our method with those of other methods [6, 37] and enlarge the local details.

7. Additional Experiments

In this section, we provide detailed performance metrics of subdivision rendering across different scenarios for further reference. Furthermore, we visualize the rendering results for both D-NeRF [31] and KITTI [24] scenarios separately.

7.1. Monocular Synthetic Scene.

We test the 8 scenes of D-NeRF [31] dataset. Due to the simple motion patterns and uniform lighting conditions in the synthesized dataset, there are insignificant differences among the different rendering techniques. Nonetheless, SDD-4DGS achieves a PSNR rendering quality of 34.82, exceeding the previous best of 34.41 as shown in Tab. 6. Additionally, it attained a rendering speed of 85.3 frames per second at a resolution of 800×800 . The static-dynamic aware decoupling reconstruction strategy prevents occlusions in dynamic segments from causing blurring or loss of details in static components. This method facilitates better capture of intricate textures in stationary regions, as illustrated in Fig. 10. For areas exhibiting minimal or slight motion, SDD-4DGS guarantees high-quality reconstruction of dynamic parts while effectively characterizing fine features such as the textures of stationary clothing and the edges of rigid structures.

Efficiency Experiment: We evaluated the FPS and training time of various baseline algorithms on the D-nerf

dataset. All experiments were conducted in a unified environment using a single NVIDIA RTX 3090 GPU for training and rendering. Since 4DRotor [6] did not release its CUDA implementation, we used its Torch version for comparison. The experimental results indicate that Spacetime [19] achieves the fastest training speed and the highest FPS due to its efficient polynomial fitting approach. Other algorithms exhibit negligible differences in training time and FPS. Additionally, for 4DGS [37], the inclusion of dynamic-static awareness mechanisms results in a reasonable increase in training time.

7.2. Multi-view Real-world Scene.

We employ the Neu3D’s [17] dataset as the benchmark for evaluating our method in real-world settings. The Neu3D’s [17] dataset includes multi-view videos of six real-world scenes featuring flowing liquids and reflective materials. We selected five scenes from this dataset and used point clouds generated by COLMAP as the initialization conditions for these scenes.

Our results, summarized in Tab. 7, demonstrate that our SDD-4DGS achieves superior rendering quality compared to other baseline approaches across diverse scenarios and on average. This performance is particularly pronounced in Scene *Coffee Martini*, where daylight conditions introduce a complex interplay of light and shadow, presenting

Table 7. **Quantitative results on the multi-view real dataset Neu3D’s [17].** The **best** results are highlighted in bold. The rendering resolution is set to 1352×1014 .

Neu3D’s	Coffee Martini			Cook Spinach			Cut Roasted Beef		
	PSNR (dB) \uparrow	SSIM \uparrow	LPIPS \downarrow	PSNR (dB) \uparrow	SSIM \uparrow	LPIPS \downarrow	PSNR (dB) \uparrow	SSIM \uparrow	LPIPS \downarrow
4DGS [37]	27.31	0.904	0.134	31.80	0.944	0.112	32.16	0.944	0.119
RealTime4DGS [43]	27.75	0.915	0.118	32.31	0.954	0.089	33.35	0.957	0.087
Spacetime [19]	27.99	0.908	0.133	30.53	0.940	0.123	30.89	0.941	0.128
4DRotor [6]	28.11	0.912	0.127	32.29	0.950	0.099	32.44	0.951	0.097
SDD-4DGS (Ours)	29.03	0.917	0.112	32.83	0.954	0.089	33.20	0.955	0.094

Neu3D’s	Flame Steak			Sear Steak			Mean		
	PSNR (dB) \uparrow	SSIM \uparrow	LPIPS \downarrow	PSNR (dB) \uparrow	SSIM \uparrow	LPIPS \downarrow	PSNR (dB) \uparrow	SSIM \uparrow	LPIPS \downarrow
4DGS [37]	31.87	0.946	0.106	32.98	0.950	0.105	31.23	0.938	0.115
RealTime4DGS [43]	32.63	0.961	0.077	33.14	0.964	0.076	31.84	0.950	0.089
Spacetime [19]	30.18	0.944	0.114	32.26	0.952	0.102	30.37	0.937	0.120
4DRotor [6]	33.11	0.958	0.085	32.72	0.958	0.086	31.73	0.946	0.099
SDD-4DGS (Ours)	32.94	0.961	0.076	33.98	0.962	0.078	32.39	0.950	0.090

Table 8. **Quantitative results on the multi-view real dataset KITTI [24].** Scenes are classified by High Dynamic Range (LDR) and Low Dynamic Range (LDR) imaging conditions with fixed cameras (FC) or moving cameras (MC). The **best** results are highlighted in bold. The rendering resolution is set to 1242×375 .

KITTI	Scene 1 (LDR & MC)			Scene 2 (LDR & FC)			Scene 3 (LDR & FC)		
	PSNR (dB) \uparrow	SSIM \uparrow	LPIPS \downarrow	PSNR (dB) \uparrow	SSIM \uparrow	LPIPS \downarrow	PSNR (dB) \uparrow	SSIM \uparrow	LPIPS \downarrow
4DGS [37]	26.27	0.894	0.099	29.10	0.939	0.054	16.09	0.421	0.450
RealTime4DGS [43]	23.44	0.804	0.348	23.50	0.783	0.174	17.55	0.672	0.312
Spacetime [19]	27.12	0.887	0.107	27.77	0.896	0.090	18.09	0.752	0.253
4DRotor [6]	19.16	0.675	0.277	10.20	0.344	0.876	8.69	0.371	0.648
SDD-4DGS (Ours)	26.77	0.901	0.089	29.80	0.948	0.044	23.54	0.925	0.063

KITTI	Scene 4 (HDR & MC)			Scene 5 (LDR & MC)			Mean		
	PSNR (dB) \uparrow	SSIM \uparrow	LPIPS \downarrow	PSNR (dB) \uparrow	SSIM \uparrow	LPIPS \downarrow	PSNR (dB) \uparrow	SSIM \uparrow	LPIPS \downarrow
4DGS [37]	14.65	0.549	0.694	20.15	0.769	0.179	21.25	0.71	0.30
RealTime4DGS [43]	17.63	0.651	0.311	19.07	0.702	0.447	20.24	0.72	0.32
Spacetime [19]	16.16	0.613	0.627	19.44	0.723	0.210	21.72	0.77	0.26
4DRotor [6]	16.63	0.593	0.746	15.11	0.506	0.303	13.96	0.498	0.570
SDD-4DGS (Ours)	21.11	0.870	0.119	20.97	0.788	0.158	24.44	0.89	0.09

significant challenges for most methods. Daytime indoor scenes are heavily influenced by natural light, with variations in sunlight intensity, angle, and diffuse light distribution leading to intricate global illumination effects and localized highlights. These phenomena compromise color consistency and hinder the recovery of geometric details during reconstruction. Moreover, strong direct sunlight often causes specular reflections and glare on reflective surfaces such as glass, metal, and tiles, further distorting color information and inducing depth map noise and data loss. Despite these challenges, our method achieves substantial improvements over the previous state-of-the-art (SOTA), demonstrating its robustness in complex scenarios.

7.3. Monocular Real-World Urban Scene.

We extended the KITTI [24] dataset to explore the applicability of Gaussian Splatting [14] technology in real urban

environments, particularly within autonomous driving applications. Compared to indoor data, urban datasets typically face challenges such as more intense natural lighting, restricted camera viewpoints, significant variations in camera poses, and motion blur along with sparse observations due to fast-moving objects. SDD-4DGS demonstrates superior performance compared to other baseline methods in handling scenes with numerous dynamic components and static backgrounds, particularly in terms of overall image quality metrics such as PSNR and SSIM in Tab. 8. Additionally, some baseline methods may experience training failures under extreme conditions. SDD-4DGS demonstrated an exceptional ability to preserve details in dynamic objects, such as vehicles. As illustrated in Fig. 11, SDD-4DGS maintained sharp edges and textural details closely matching the ground truth, essential for accurate vehicle

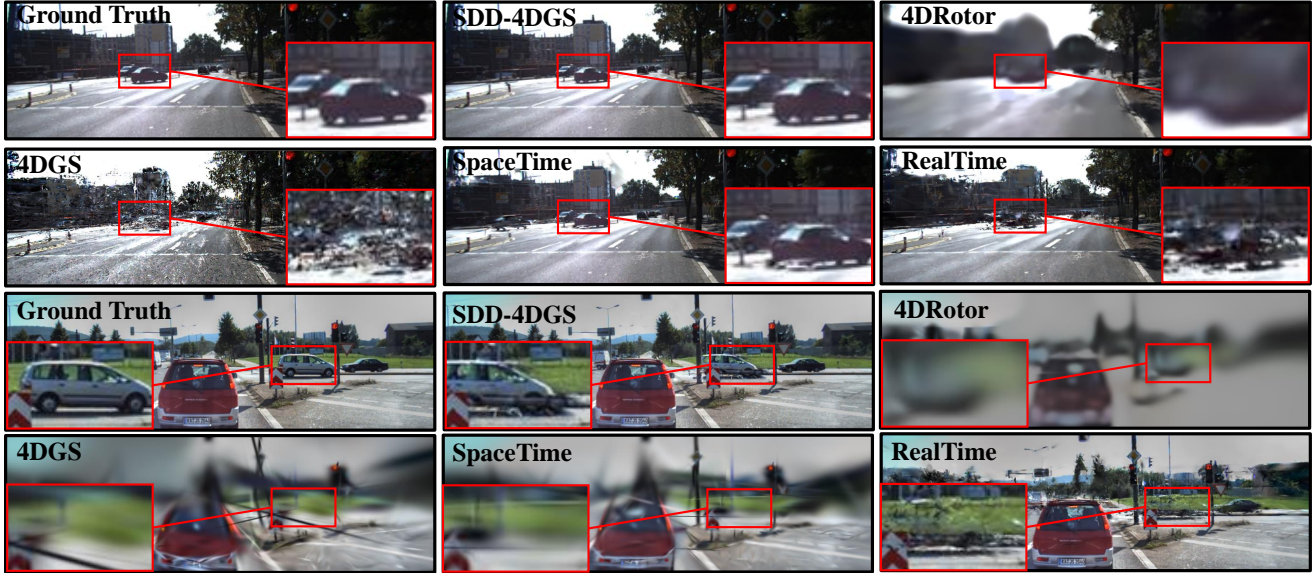


Figure 11. **Comparative visualization of Gaussian splatting techniques on the KITTI [24] dataset.** The images highlight SDD-4DGS’s enhanced detail preservation in dynamic objects like vehicles, closely matching the ground truth with sharp edges and accurate textures. In contrast, baseline methods such as 4DGS and SpaceTime show significant blurring and artifacts. These results demonstrate the robustness of SDD-4DGS against the challenges of intense outdoor lighting and motion blur, underscoring its potential for reliable vehicle detection and tracking.

detection and tracking. In contrast, methods like 4DGS and SpaceTime exhibited significant blurring and artifacts around moving cars, which could detrimentally impact the performance of perception systems in autonomous vehicles.

7.4. Automatic Supervision Signal

To facilitate effective static-dynamic decoupling in 4D reconstruction, we introduce an uncertainty-based automatic supervision signal [16] that generates binary masks to guide the optimization process. This approach builds upon the observation that dynamic regions typically exhibit higher uncertainty during reconstruction due to their time-varying nature.

Motion Mask Generation The key challenge in deriving supervision signals for static-dynamic decoupling lies in automatically identifying which regions in each frame correspond to dynamic or static components without explicit annotations. We address this through an uncertainty estimation mechanism that leverages the semantic consistency properties of pre-trained visual features. Specifically, we utilize DINOv2 [26] to extract patch-level features from both rendered and ground truth images. These features exhibit remarkable robustness to illumination changes while remaining sensitive to geometric inconsistencies—a critical property for distinguishing between static structures and dynamic objects. For each image pair, we define the uncertainty score σ through a linear mapping of feature similar-

ity:

$$\mathcal{L}_{uncertainty} = \min(1, 2 - 2 \cos(\tilde{D}, D)) \frac{1}{2\sigma^2} + \lambda_{prior} \log \sigma \quad (13)$$

, where \tilde{D} and D represent the DINOv2 features extracted from patches of the rendered and training images, respectively, with $\cos(\tilde{D}, D)$ denoting the cosine similarity between these features vectors. The term $\lambda_{prior} \log \sigma$ serves as a regularization prior to prevent uncertainty collapse.

The uncertainty scores are optimized independently from the main reconstruction parameters to prevent gradient interference, ensuring that the densification algorithm in the Gaussian splatting pipeline maintains its effectiveness. After obtaining the optimized σ values, we convert them into binary masks using:

$$m = \mathbb{1} \left(\frac{1}{2\sigma^2} > 1 \right) \quad (14)$$

, where $\mathbb{1}$ is the indicator function that evaluates to 1 when $\sigma^2 < \frac{1}{2}$. This approach effectively identifies dynamic regions (where $m = 1$) without requiring explicit motion annotations. Additional details can be found in [16].